

Coupled Residual Stiffness and Strength Model for Fatigue of Fibre-reinforced Composite Materials

W. Van Paepegem* and J. Degrieck

Ghent University, Dept. of Mechanical Construction and Production,
Sint-Pietersnieuwstraat 41, 9000 Gent, Belgium

Abstract

The fatigue behaviour of fibre-reinforced composite materials is complex and present knowledge is far from complete. Several classes of models attempt to predict the fatigue life and/or fatigue degradation of fibre-reinforced composites. Two major classes are the residual stiffness models and the residual strength models. This paper presents a phenomenological residual stiffness model which predicts the stiffness degradation as well as final failure of the composite component. The reserve to failure has been evaluated by means of a modified use of the Tsai-Wu static failure criterion. The fatigue damage model has been applied to displacement-controlled bending fatigue experiments of plain woven glass/epoxy specimens. The damage and stress (re)distribution, as well as the force-cycle history have been simulated and compared to experimental results. Due to the consistent integration of continuum damage mechanics and the residual stiffness approach, the implementation of the fatigue model in a commercial finite element code has been possible, which allows for an accurate simulation of the successive damage states during fatigue life.

Keywords A: Textile composites; B: Fatigue; C: Damage mechanics; C: Finite element analysis (FEA); C: Failure criterion.

1. Introduction

The fatigue behaviour of fibre-reinforced composite materials has been studied for many years, and although the underlying damage mechanisms are understood quite well, there does not exist so far any fatigue model that can be applied to a wide range of fibre-reinforced composites under a variety of fatigue loading conditions. Nevertheless a broad range of fatigue models have been developed, amongst which the residual stiffness and residual strength models make up the most important class [1].

Although the residual strength models are able to predict the moment of final failure (when the residual strength equals the applied stress), they cannot simulate the stiffness degradation and inherent stress redistribution. On the other hand, residual stiffness models lack the ability to predict final failure, because there is no correlation between stiffness and final failure in the classical residual stiffness approach. In this paper, a fatigue damage model is presented that is based on the residual stiffness approach. Through a modified use of the Tsai-Wu static failure criterion, a fatigue failure index is defined which is a measure for the applied nominal stress, but at the same time reflects the reserve to failure under increasing fatigue damage. The fatigue damage model can describe the three stages in the stiffness degradation curve (sharp initial decline – gradual degradation – final failure). In order to accurately simulate these

* Corresponding author (Fax: +32-(0)9-264.35.87, E-mail: Wim.VanPaepegem@rug.ac.be).

stages in fatigue life, the fatigue damage model is implemented in a commercial finite element code. As such, the stiffness, damage and stress distribution can be assessed at successive damage states during fatigue life.

2. Materials and experimental setup

The material used in the bending fatigue experiments, was a glass fabric/epoxy composite. The fabric was a Roviglass R420 plain woven glass fabric (Syncoglas) and the epoxy was Araldite LY 556 (Ciba-Geigy). The plain woven glass fabric was stacked in eight layers, denoted as $[\#0^\circ]_8$, where '0°' means that the warp direction of each of the eight layers has been aligned with the loading direction and where the symbol '#' refers to the fabric reinforcement type. All composite specimens were manufactured using the resin-transfer-moulding technique. After curing they had a thickness of 2.72 mm. The samples were cut to dimensions of 145 mm long by 30 mm wide on a water-cooled diamond saw. The fibre volume fraction V_f was 0.48.

The experimental results were obtained from displacement-controlled cantilever bending fatigue experiments. One side of the specimen was clamped, while a sinusoidal displacement was imposed at the other side of the specimen. Figure 1 shows a schematic drawing.

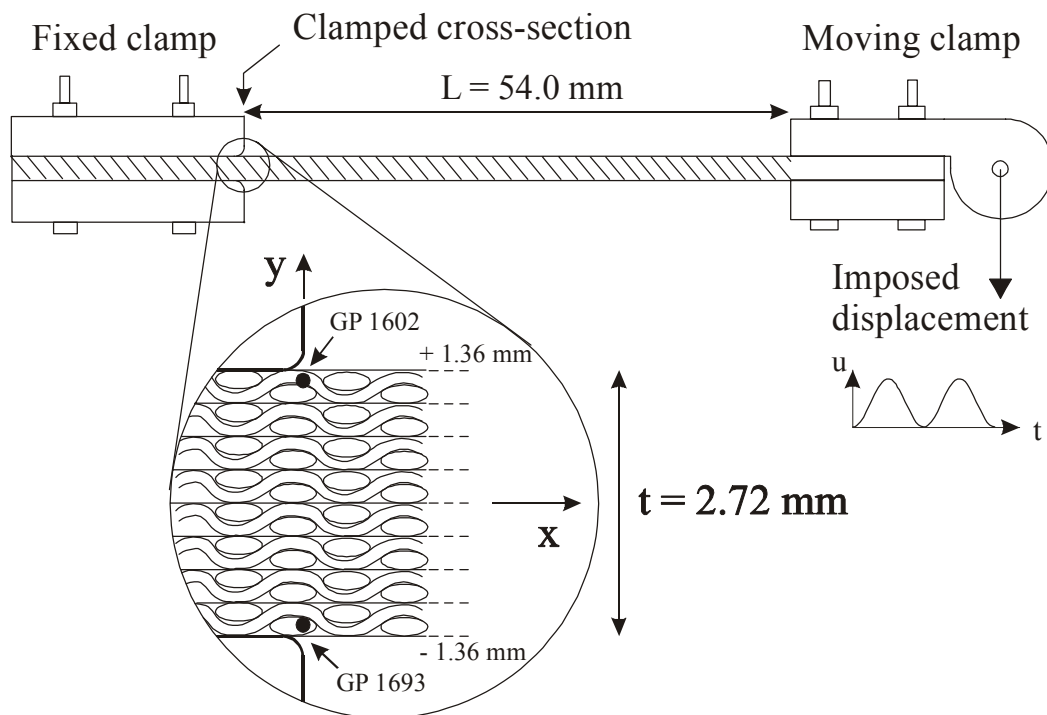


Figure 1 Schematic drawing of the bending fatigue setup.

The testing frequency was fixed at 2.2 Hz. The amplitude u_{\max} of the imposed displacement is a controllable parameter and the displacement ratio R_d (analogous to the stress ratio R) is defined as $R_d = u_{\min}/u_{\max}$. For single-sided bending the displacement ratio $R_d = 0.0$, which means also that the stress ratio R is zero for each point in the composite specimen. Of course, due to the varying bending moment, and the varying stresses and strains along the length and

through the thickness of the specimen, the maximum stress amplitude will generally be different in each material point.

3. Layout of the fatigue damage model for single-sided bending

Recently, the authors proposed a new fatigue damage model that is capable of simulating the three stages in stiffness degradation (sharp initial decline – gradual deterioration – final failure) [2,3]. This phenomenological model is valid for uni-axial loading of delamination-free specimens with zero stress-ratio $R = \sigma_{\min}/\sigma_{\max}$.

The model is one-dimensional in nature, and the only acting stress component is σ_{11} . Since the warp direction of each layer of the $[\#0^\circ]_8$ glass/epoxy laminate is aligned with the loading direction, the orthotropic stress σ_{11} coincides with the resulting stress σ_{xx} from the bending fatigue test, and the orthotropic elastic property E_{11} corresponds with the longitudinal stiffness. In the following discussion, the stress σ_{11} in the one-dimensional model will be further designated with the symbol σ . The stiffness E_{11} will be further designated as the stiffness E , where E_0 is the initial modulus of the undamaged homogenized material.

As already mentioned, the model is based on the residual stiffness approach. Hence stress and strain are related by the commonly used equation in continuum damage mechanics:

$$\tilde{\sigma} = \frac{\sigma}{1-D} = E_0 \varepsilon \quad (1)$$

where $\tilde{\sigma}$ is the effective stress, σ is the applied nominal stress, ε is the nominal strain, E_0 is the undamaged Young's modulus and D is a measure for the fatigue damage. The scalar damage variable D , defined as $D = 1 - E/E_0$, is a macroscopic measure for the fatigue damage, since the structural changes on the microscopic scale (matrix cracks, fibre/matrix interface failure,...) are characterized by a macroscopic reduction of the stiffness. The value of D is lying between zero (virgin material state) and one (final failure).

In order to establish now a relation between the residual stiffness and the reserve to failure, the Tsai-Wu static failure criterion is used in a different manner. The actual effective stress $\tilde{\sigma}$ is inserted in the commonly used Tsai-Wu criterion and the reserve factor R to failure is calculated from the equation:

$$\left[\left(\frac{\sigma}{1-D} \right)^2 \frac{1}{X_T \cdot |X_C|} \right] R^2 + \left[\frac{\sigma}{1-D} \left(\frac{1}{X_T} - \frac{1}{|X_C|} \right) \right] R - 1 = 0 \quad (2)$$

where X_T and X_C are the static tensile and compressive strength, respectively.

The fatigue failure index $\Sigma(\sigma, D)$ is then defined as the inverse of the reserve factor R . Hence the fatigue failure index is the ratio of the applied effective stress $\tilde{\sigma}$ to the initial static strength. This measure for the applied stress in relation with the static strength will now be used in the damage growth rate equation dD/dN that is given by [2,3]:

$$\frac{dD}{dN} = \begin{cases} c_1 \cdot \Sigma \cdot \exp\left(-c_2 \frac{D}{\sqrt{\Sigma}}\right) + c_3 \cdot D \cdot \Sigma^2 \cdot [1 + \exp(c_5(\Sigma - c_4))] & \text{if } \sigma \geq 0 \\ \left[c_1 \cdot \Sigma \cdot \exp\left(-c_2 \frac{D}{\sqrt{\Sigma}}\right) \right]^3 + c_3 \cdot D \cdot \Sigma^2 \cdot \left[1 + \exp\left(\frac{c_5}{3}(\Sigma - c_4)\right) \right] & \text{if } \sigma < 0 \end{cases} \quad (3)$$

For both tensile and compressive regime, two separate terms in the damage evolution law can be distinguished. The first term accounts for damage initiation, but once that damage is growing, the exponential function forces the first term to disappear, and the second term becomes the predominant one. The latter describes the damage propagation phase. This distinction between damage initiation and propagation has been inspired by the typical stiffness degradation behaviour: a sharp initial decline, followed by a gradual degradation. The growth rate is different in tension and compression, because it has been observed from the experimental fatigue tests that compressive damage growth rate is much smaller under the following restrictive conditions:

- the displacement ratio $R_d = 0.0$, which means that the bending experiments are single-sided. As a consequence, each material point is subjected to stresses which do not change sign during one cycle. Because $u_{\min} = 0.0$, the stress ratio R is zero for all the material points involved,
- there are no delaminations. Due to the chosen stacking sequence, no delaminations have been observed.

All five constants c_i ($i = 1, \dots, 5$) have a distinctive meaning:

- c_1 regulates the growth rate of the damage initiation regime (and thus the sharp initial decline of the modulus degradation curve),
- c_2 is sufficiently large, so that the first term is disappearing as damage increases. Then, the “Characteristic Damage State” of matrix cracking [4-6] has been reached,
- c_3 represents the growth rate in the propagation phase of modulus degradation, where additional damage mechanisms (fibre/matrix interface failure, fibre pull-out) lead to a gradual decline of the stiffness,
- c_4 and c_5 express the explosive damage growth once that the fatigue failure index $\Sigma(\sigma, D)$ approaches its failure value 1.0, and the effective stress $\tilde{\sigma}$ reaches the static strength in tension or compression.

The parameters c_i ($i=1, \dots, 5$) have been determined from a “standard” bending fatigue test with the displacement amplitude $u_{\max} = 30.4$ mm [2,3]. Their values are listed in Table 1, together with the elastic and strength properties. The in-plane elastic properties of the $[\#0^\circ]_8$ composite laminates were determined using the dynamic modulus identification method described by Sol et al. [7,8]. The values in Table 1 will be used for all subsequent simulations.

Table 1 Material and model constants.

Material parameters		Model parameters	
E_{11} [GPa]	24.57	c_1 [1/cycle]	0.002
E_{22} [GPa]	23.94	c_2 [-]	30.0
ν_{12} [-]	0.153	c_3 [1/cycle]	$4.0 \cdot 10^{-6}$
G_{12} [GPa]	4.83	c_4 [-]	0.85
X_T [MPa]	390.7	c_5 [-]	93.0
X_C [MPa]	345.1		

It is important to note that the application of the fatigue damage model (Eq. (3)) is not limited to the simulation of bending fatigue experiments, although the fatigue damage model was

developed and validated for bending fatigue tests. As the fatigue model pretends to be a true material model, i.e. intrinsic to the material used, it is able to predict the stiffness degradation in each material point for any applied uni-axial nominal stress σ which can change during fatigue life and which might be different in each material point. However bending fatigue experiments were preferred because each material point through the thickness sustains a different stress amplitude σ (due to the bending moment), so that the fatigue damage model could be tested for a wide range of tensile and compressive stress amplitudes. Moreover, due to the stress redistribution, the stress amplitude in the material points changes during fatigue life, and a sort of variable-amplitude loading is simulated. These advantages support the choice of simple bending experiments as a powerful validation experiment for the model developed.

To prove that the model can indeed be used for all types of uni-axial loading conditions and to make the reader feel acquainted with the behaviour of the proposed fatigue damage model, a simple numerical example is given first for a uni-axial tension fatigue test.

4. Illustrative numerical simulation

The model has been applied to a load- and strain-controlled tension fatigue test to show the influence of the fatigue failure index and its major role as a driving force in damage growth. For both types of tests, the minimum stress level is zero (stress ratio $R = 0$) and the applied maximum stress σ in the first cycle is 60 % of the static strength X_T and equals 234.4 MPa (see Table 1). This means that for the load-controlled fatigue tests, the nominal maximum stress σ remains equal to 234.4 MPa during fatigue, while the strain for the strain-controlled fatigue tests is fixed at a value of 0.954 %. Calculations have been done for 200,000 cycles. Figure 2 shows the stiffness degradation curve for the load- and strain-controlled tensile fatigue test. For the load-controlled fatigue test, the three distinctive stages in fatigue life are simulated and final failure is predicted at about 110,000 cycles. For the strain-controlled fatigue test, the stiffness degradation remains more gradual and since the applied strain is well below the static failure strain, final failure does not occur yet. As $D = 1 - E/E_0$, the damage curves can be easily derived from the stiffness degradation curves in Figure 2.

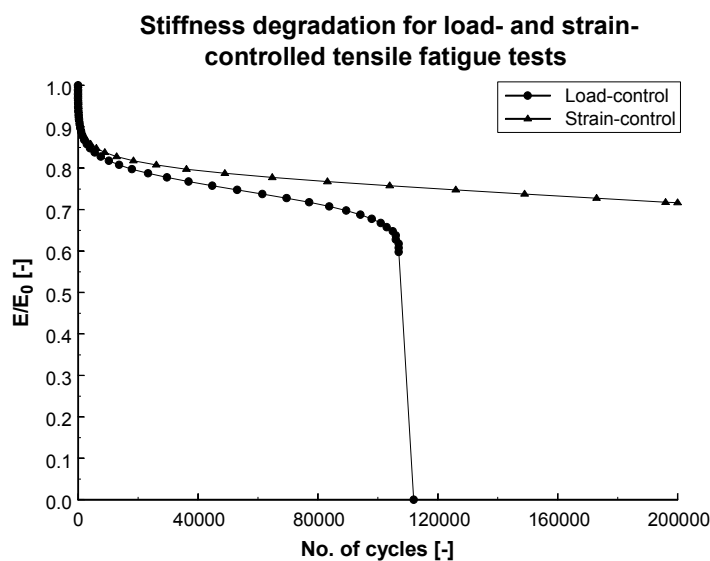


Figure 2 Stiffness degradation curve for load- and strain-controlled tension fatigue tests ($R=0$).

Figure 3 shows the behaviour of the fatigue failure index $\Sigma(\sigma, D)$ during fatigue life. As the applied stress in the first loading cycle was equal to 60 % of the static strength, the failure index equals 0.60 in the first loading cycle for each type of fatigue test (fatigue damage $D = 0$). However, when damage is accumulating, the effective stress $\tilde{\sigma}$ ($= \sigma/(1-D)$) is increasing for the load-controlled fatigue tests. When the fatigue failure index reaches its failure value 1.0, final failure occurs and the stiffness falls down to zero. For the strain-controlled fatigue test, the effective stress $\tilde{\sigma}$ ($= E_0 \varepsilon$) is constant and once the initiation term has diminished, the damage growth rate dD/dN is roughly proportional to the factor $c_3 \cdot D \cdot \Sigma^2$ (see Eq. (3)). In this case, failure will occur when the damage D reaches its failure value 1.0. Due to the small propagation rate of dD/dN , fatigue life will be considerably larger than for the load-controlled fatigue test.

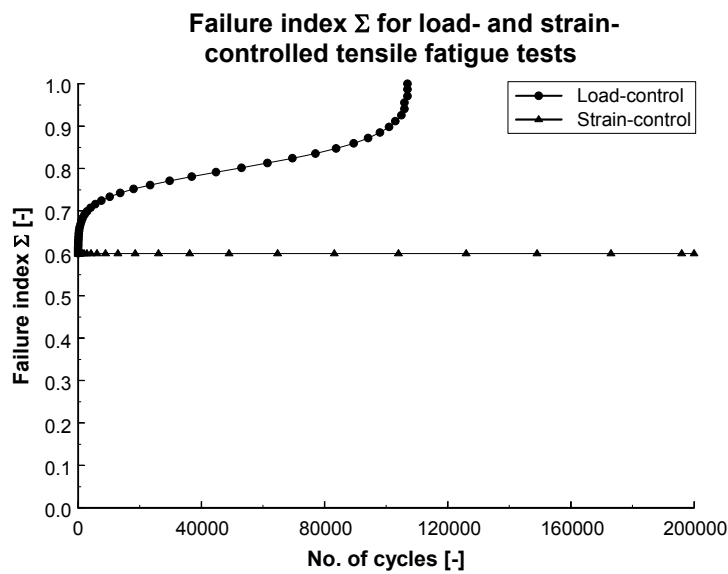


Figure 3 Fatigue failure index Σ for the load- and strain-controlled fatigue tests.

Figure 4 shows the contributions of the damage initiation and damage propagation term (see Equation (3)) for the load-controlled fatigue test. It clearly appears that damage initiation and damage propagation are indeed properly described by the two separate terms in Equation (3). As both terms are expressed as damage growth rates *per cycle*, the values are of course very small.

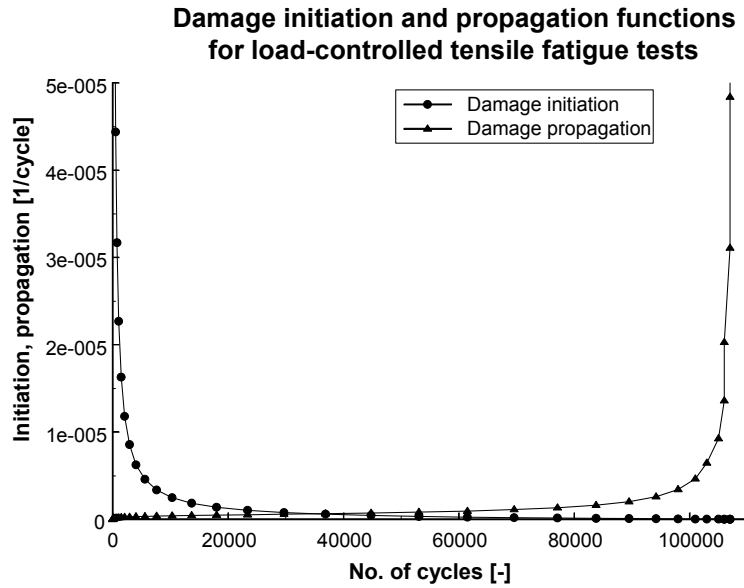


Figure 4 Contributions of damage initiation and propagation for load-controlled testing.

It can be concluded from Figure 5 that the damage propagation term is a lot smaller for the strain-controlled fatigue tests. Therefore a different scale has been used for the damage propagation term.

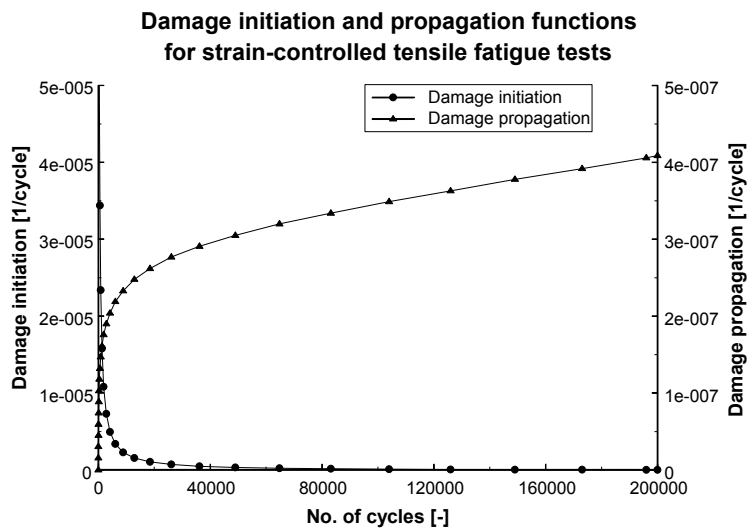


Figure 5 Contributions of damage initiation and propagation for strain-controlled testing.

It is obvious to say that in the last stage of the stiffness degradation curve, a transfer to localized damage progression occurs, leading to a simple or multiple strand failure which results in a sudden drop of the characteristic stiffness reduction curve and which initiates final failure. This is a reason for the large scatter in fatigue life, making that the sudden final drop in stiffness can hardly be predicted [4]. However it is not that important that the exact moment of final failure can be predicted, because this depends on small variations in mechanical properties. Yet it is very important that the damage growth law is capable of simulating this

catastrophic failure behaviour. Indeed, then it can be assessed whether this localized failure will lead to a complete collapse of the structural component, or stress redistribution will be able to prevent the localized failure event from leading to final failure of the whole composite structure.

In the next paragraph simulations of bending fatigue experiments will be discussed and there again, it will be shown that it is very important that the damage growth law is capable of simulating the stage of final failure.

5. Finite element results for single-sided bending

The fatigue damage model has been implemented in the commercial finite element code SAMCEFTM. The finite element mesh for the bending fatigue tests is shown in Figure 6. The composite specimen was modelled by 3-D isoparametric ‘brick’ elements. The clamping plates of the fixation were included in the model, and the prescribed displacement u_{\max} was imposed at the tip of the rigid body element representing the moving clamp.

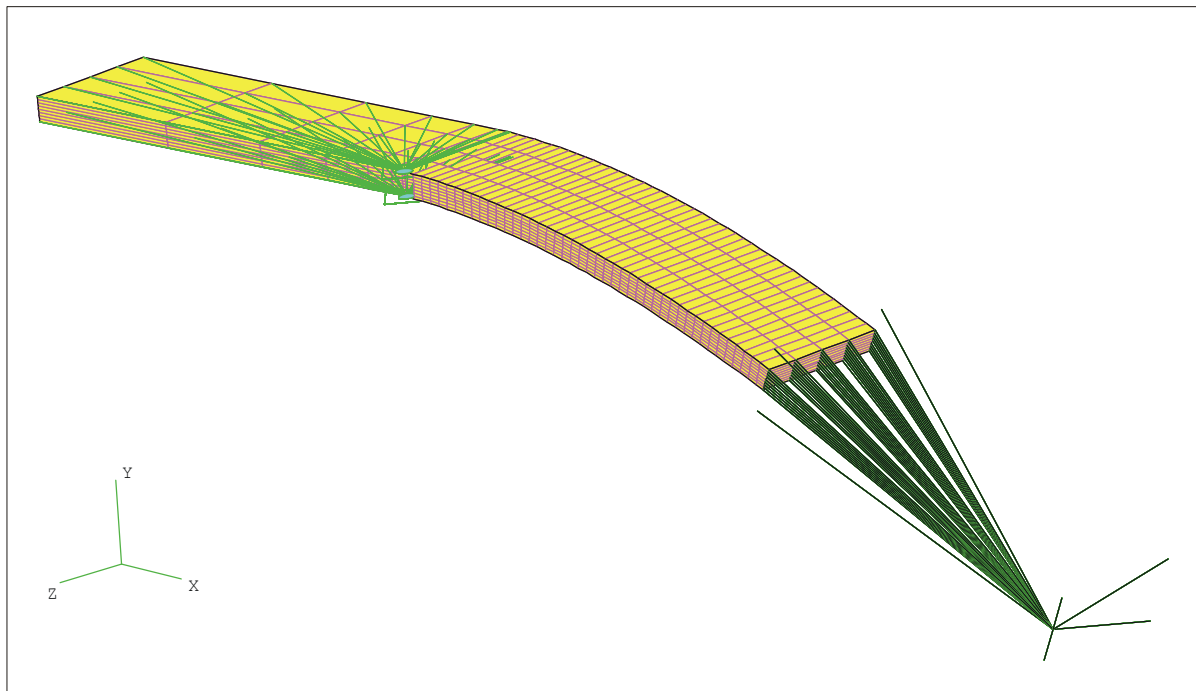


Figure 6 Finite element mesh for the displacement-controlled bending fatigue tests.

The integration of the damage growth rate equation dD/dN (Equation (3)) for each Gauss-point has been done with the *cycle jump* approach which has been recently proposed by the authors [9]. Briefly the *cycle jump* approach means that the computation is done for a certain set of loading cycles at deliberately chosen intervals, and that the effect on the stiffness degradation of these loading cycles is extrapolated over the corresponding intervals in an appropriate manner. To this purpose, each Gauss-point has been assigned – besides the damage variable D – a second state variable N_{JUMP1} , which is the number of cycles that could be jumped over without losing reliability and accuracy for that particular Gauss-point. After looping over all Gauss-points, a cumulative relative frequency distribution of the

NJUMP1 values is calculated and an overall cycle jump NJUMP (which will be applied to the whole finite element mesh) is determined as a percentile of this frequency distribution.

The local cycle jump NJUMP1 is defined by imposing a maximum allowable increase in damage ΔD for each particular Gauss-point when the calculation would proceed for NJUMP1 cycles. When the increase ΔD is limited to for example 0.01, this is equivalent to a piece-wise integration of the damage evolution law for that Gauss-point by dividing the ordinate axis of the damage-cycle history into 100 segments. By decreasing the upper threshold for ΔD for each Gauss-point, the damage evolution law dD/dN will be integrated more accurately, but the global NJUMP – a percentile of the cumulative frequency distribution of all NJUMP1 values – will be smaller and the calculation will proceed more slowly.

The parameters for the fatigue damage model (listed in Table 1) were determined from the “standard” fatigue test “Pr05_2”. Figure 7 shows the experimental and simulated force-cycle history. The frequency was 2.2 Hz and the imposed displacement varied between zero (stress ratio $R = 0.0$ for all Gauss-points) and $u_{\max} = 30.4$ mm. The force was experimentally measured by a strain gauge bridge and represents the force that is necessary to impose the bending displacement with constant amplitude u_{\max} . Due to the (bending) stiffness degradation, this force decreases during fatigue life.

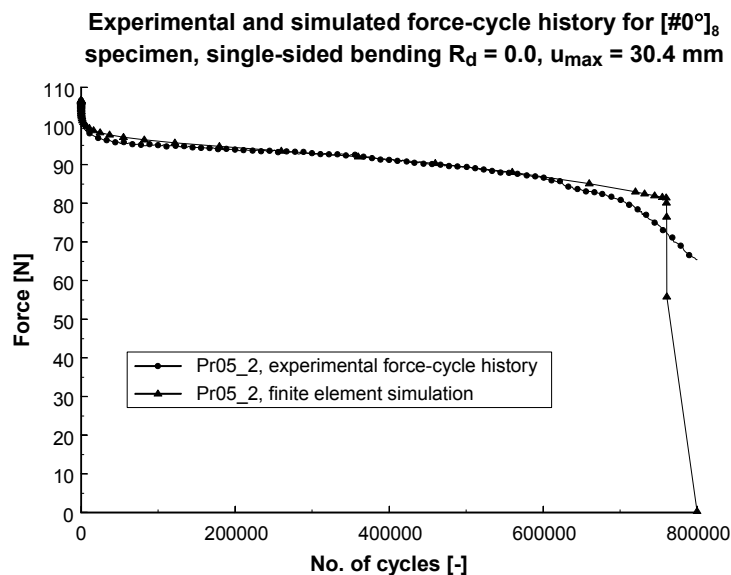


Figure 7 Experimental and simulated force-cycle history for the “standard” fatigue test.

The fatigue damage model is now applied to three other fatigue bending tests, whereby all finite element simulations are done with the material and model constants listed in Table 1. The first simulation is done for the fatigue test “Pr05_3” with $u_{\max} = 29.5$ mm. The experimental and simulated results are shown in Figure 8.

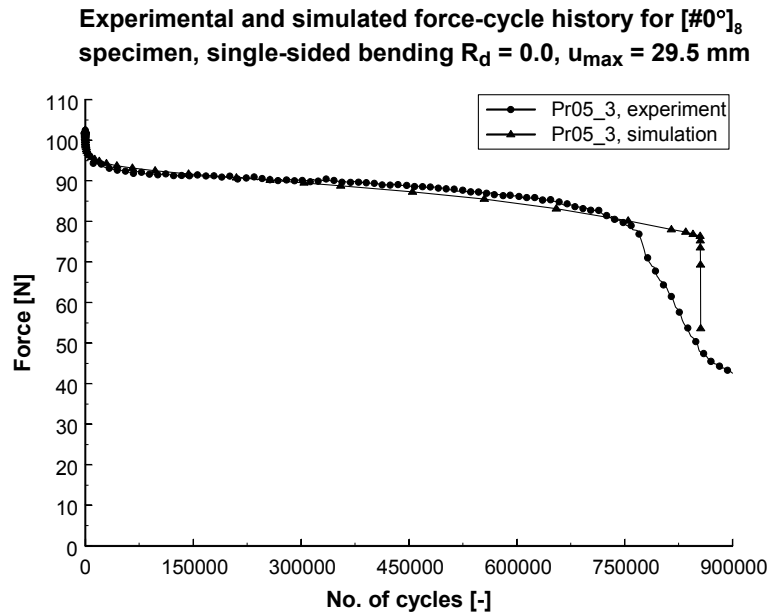


Figure 8 Experimental and simulated force-cycle history for $u_{\max} = 29.5$ mm.

As the imposed displacement u_{\max} is slightly smaller than the maximum displacement amplitude $u_{\max} = 30.4$ mm for the standard experiment “Pr05_2”, fatigue failure is predicted about 80,000 cycles later. It was observed from the fatigue experiment that final failure occurred at the tensile side, and that the compressive side was not visibly damaged at all. To check this observation, the damage value in two Gauss-points of interest will now be investigated. The Gauss-point 1602 is lying at the tensile surface, while the Gauss-point 1693 is lying at the compressive surface, both in the clamped cross-section. Their position is schematically indicated in Figure 1.

The histories of the damage variable D and the fatigue failure index $\Sigma(\sigma, D)$ are shown in Figure 9 for Gauss-point 1602. It appears that the damage variable D reaches its failure value 1.0 at about 650,000 cycles.

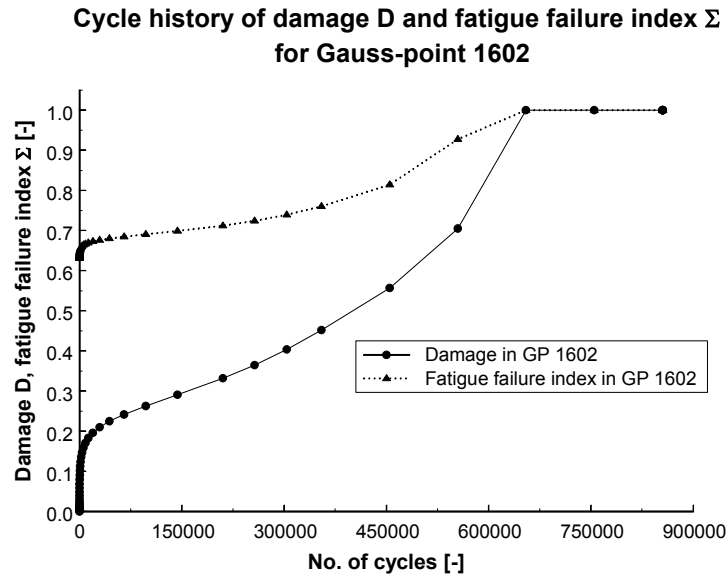


Figure 9 Damage-cycle history for the Gauss-point 1602.

Figure 10 shows the corresponding histories for Gauss-point 1693. Indeed, conform with the experimental observations, the damage at the compressive surface is still very small at the moment when the Gauss-point at the tensile side has failed ($N \approx 650,000$ cycles).

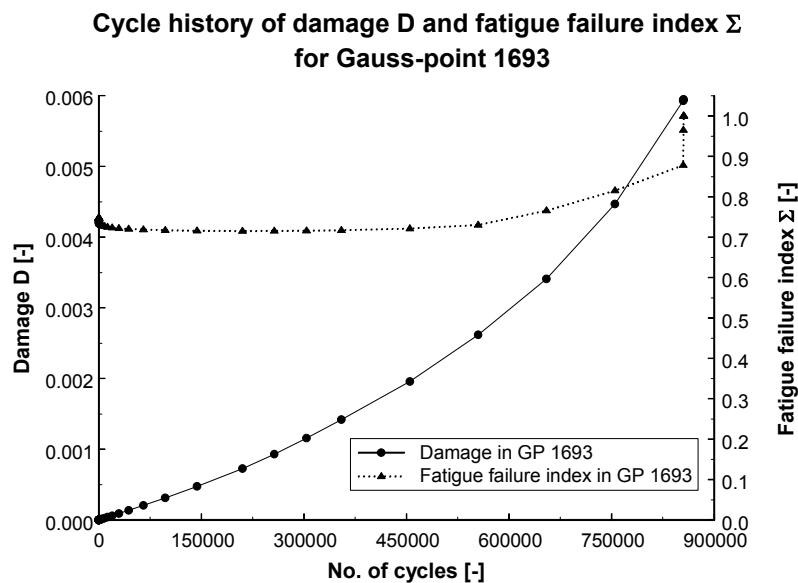


Figure 10 Damage-cycle history for the Gauss-point 1693.

From Figure 8, Figure 9 and Figure 10, it can be observed that final failure occurs only 200,000 cycles after the first Gauss-point has failed, and that just before final failure, at about

850,000 cycles, the fatigue failure index $\Sigma(\sigma, D)$ for the Gauss-point 1693 suddenly jumps to its failure value 1.0, although the fatigue damage is very small in that Gauss-point. These observations can be explained by an investigation of the stress (re)distribution at the clamped cross-section (see Figure 11). The abscissa contains the normal stress (tensile stresses are positive, compressive stresses are negative), while the ordinate axis represents the full thickness of the specimen ($y \in [-1.36 \text{ mm}, +1.36 \text{ mm}]$). At cycle $N = 1$, the stress distribution is symmetric with respect to the midplane. Of course, due to the fact that more than one element is used through the thickness and the Bernoulli assumption is no longer imposed, the stress distribution at cycle $N = 1$ is not linear, although no damage is present at that time. Also, the presence of the clamping plates disturbs the stress state at the surface near the fixation. When damage is initiating, the tensile stresses in the outermost layers are relaxed and load is transferred towards the inner layers. It can be seen that the failure of the first Gauss-point 1602 is compensated by a stress redistribution at the clamped cross-section. This is confirmed by the increase of the fatigue failure index for Gauss-point 1693 after 650,000 cycles (see Figure 10). Next final failure is initiated by the collapse of the Gauss-point lying at the tensile side and just below the Gauss-point 1602. Indeed, near the tensile surface, the stress is reduced to zero due to the complete stiffness loss. Due to the failure of these Gauss-points and the stress redistribution, the stress at the compressive surface approaches the compressive strength $X_C = -345.1 \text{ MPa}$ (see Table 1) and the associated fatigue failure index jumps to its failure value 1.0 (see Figure 10).

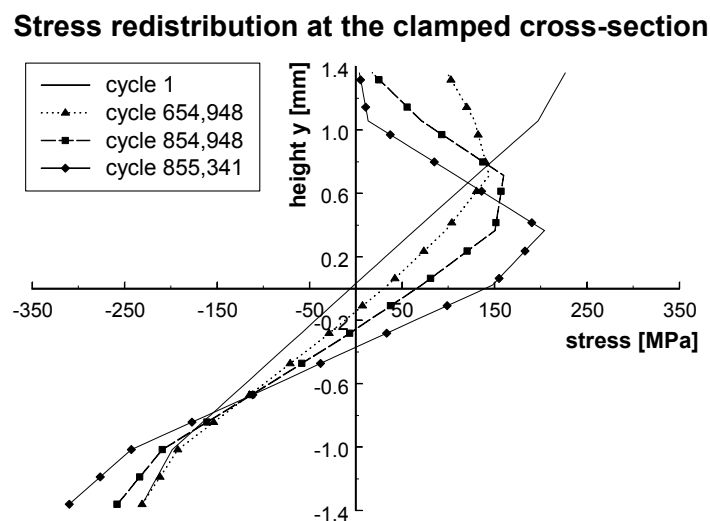


Figure 11 Stress redistribution at the clamped cross-section.

From this detailed discussion, the merit of the fatigue failure index $\Sigma(\sigma, D)$ is proved again: at the tensile side, failure is initiated through an increasing value of the damage D , and hence of the effective stress $\tilde{\sigma}$ ($=\sigma/(1-D)$) and the fatigue failure index. At the compressive surface, the damage D is very small, but due to stress redistribution, the applied nominal stress σ increases almost up to the compressive static strength, and again, the fatigue failure index indicates failure.

The next simulation is done for the fatigue test “Pr05_1” with $u_{\max} = 27.7 \text{ mm}$. The results are shown in Figure 12.

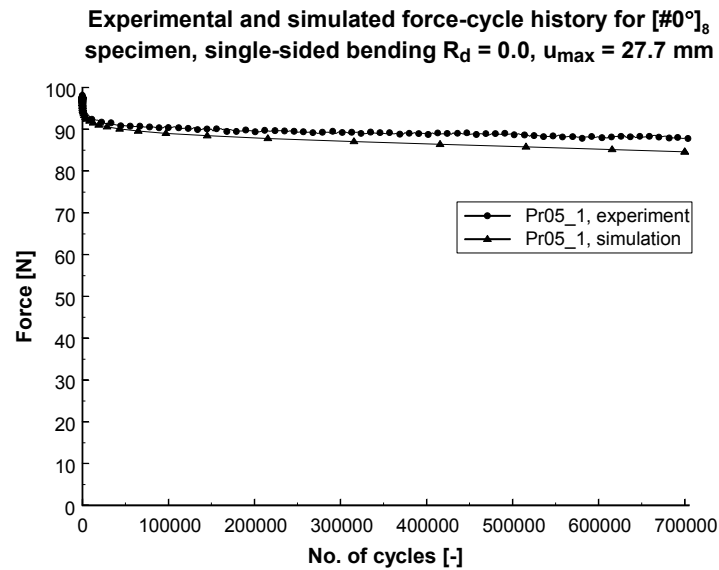


Figure 12 Experimental and simulated force-cycle history for $u_{max} = 27.7$ mm.

It is worthwhile to note that the developed *cycle jump* approach [9] works very well. In Figure 12, the *cycle jumps* correspond to the number of cycles between each of the triangle symbols on the numerically simulated force-cycle history, and each triangle symbol indicates the cycle number at which a full fatigue loading cycle has been simulated. At the first stage of sharp decline, the *cycle jumps* are very small, while during the phase of gradual degradation, the *cycle jumps* are increased up to 100,000 cycles, which results in a fast and efficient finite element simulation.

Finally the fatigue damage model is applied to the fatigue experiment “Pr08_2” with $u_{max} = 38.9$ mm. The experimental fatigue life is drastically reduced to about 25,000 cycles. The experimental and simulated force-cycle history are shown in Figure 13. Although the parameters of the fatigue damage model have been determined for a bending fatigue test with a fatigue life of about 700,000 cycles, the model predicts very well the moment of failure of this fatigue test.

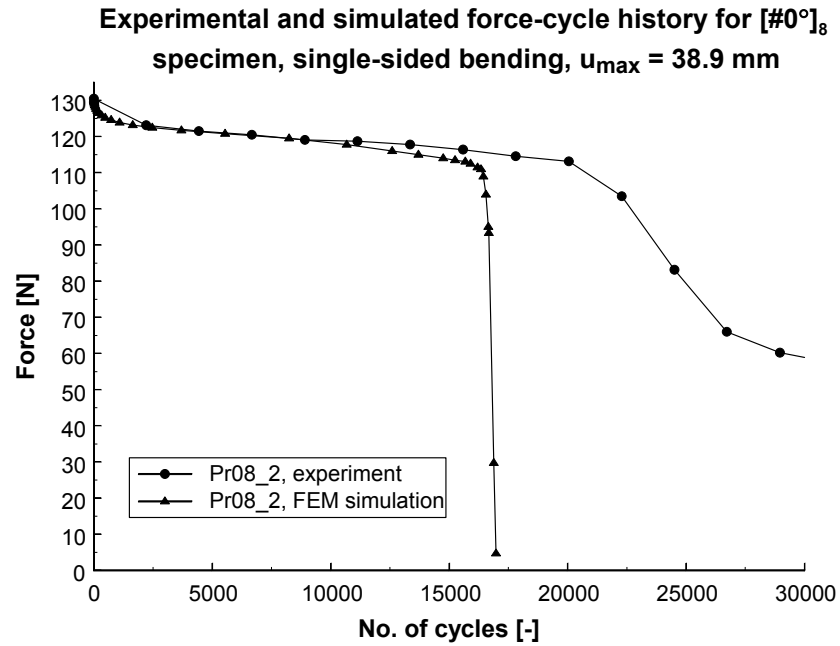


Figure 13 Experimental and simulated force-cycle history for $u_{\max} = 38.9$ mm.

As the fatigue damage model is applied to quite different loading conditions from the standard experiment “Pr05_2” ($u_{\max} = 38.9$ mm vs. $u_{\max} = 30.4$ mm) and the fatigue lives are drastically different ($N_f \approx 25,000$ cycles vs. $N_f \approx 700,000$ cycles), the finite element results of this fatigue test will be compared in more detail with the experimental results, thus aiming at a final validation of the proposed fatigue damage model.

6. Further discussion and final validation

A first indication of the correctness of the finite element results concerns the prediction of the first location of failure. For the fatigue test “Pr08_2”, it was observed that although the compressive strength was smaller, failure first occurred at the tensile side. This is confirmed by the damage-cycle history of the Gauss-points 1602 and 1693 (see Figure 1 for their respective positions).

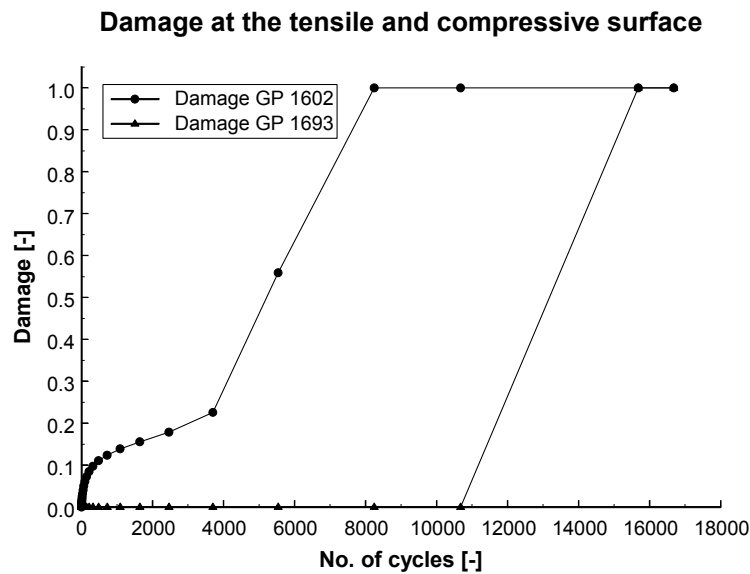


Figure 14 Damage-cycle history for the Gauss-points 1602 and 1693 in experiment “Pr08_2”.

The tensile damage is growing fast due to the high level of applied stress, while the third power of the damage initiation term for compressive stresses (see Eq. (3)) prevents the damage at the compressive side from initiating fast. The very fast increase of the damage at Gauss-point 1602 is caused by the damage propagation term in Equation (3): due to the large value of u_{\max} ($= 38.9$ mm), the initial stresses at the clamped cross-section are very high and the fatigue failure index $\Sigma(\sigma, D)$ crosses the threshold c_4 ($= 0.85$) very soon. Then the contribution of the damage propagation term is increasing exponentially and forces failure of the Gauss-point 1602. Due to the stress redistribution, the localized failure at the tensile side causes the compressive stress in the Gauss-point 1693 to increase suddenly and complete failure of the composite specimen is following soon.

A strong validation can be made by comparing the experimentally observed damage distribution along a lateral cross-section of the specimen with the predicted damage distribution. Figure 15 and Figure 16 show these predicted damage distributions at $N = 1,092$ cycles and $N = 15,681$ cycles respectively. The abscissa coincides with the length axis of the specimen: the negative x -values correspond to coordinates inside the clamping plates ($x \in [-30$ mm, 0 mm]), while the positive x -values correspond to the free specimen length ($x \in [0$ mm, 54.0 mm]). The ordinate axis represents the full thickness of the specimen ($y \in [-1.36$ mm, $+1.36$ mm]), so that the plot area covers the complete lateral cross-section of the specimen length, as schematically indicated by the diagonally dashed lateral cross-section in Figure 1. Of course, in order to present the data comprehensively, the ratio between the specimen length on the abscissa and the specimen thickness on the ordinate axis has been distorted. The contours are lines of equal damage, where the value of the damage is lying between zero (no damage) and one (complete failure).

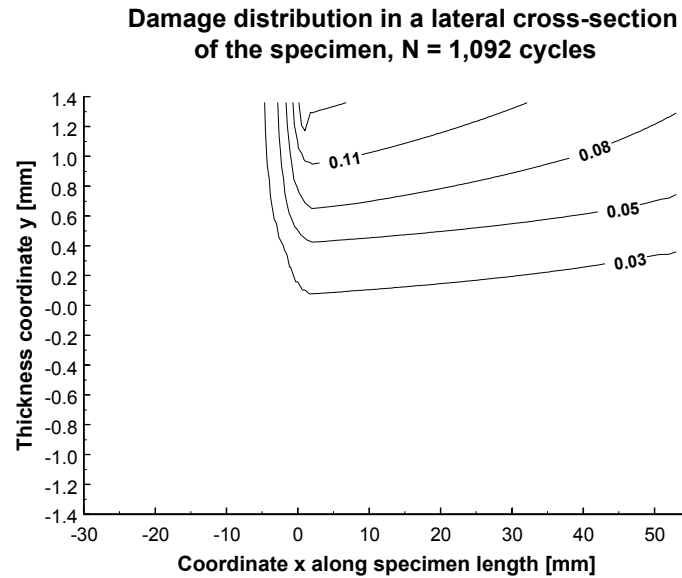


Figure 15 Damage distribution in a lateral cross-section of the specimen at N = 1,092 cycles.

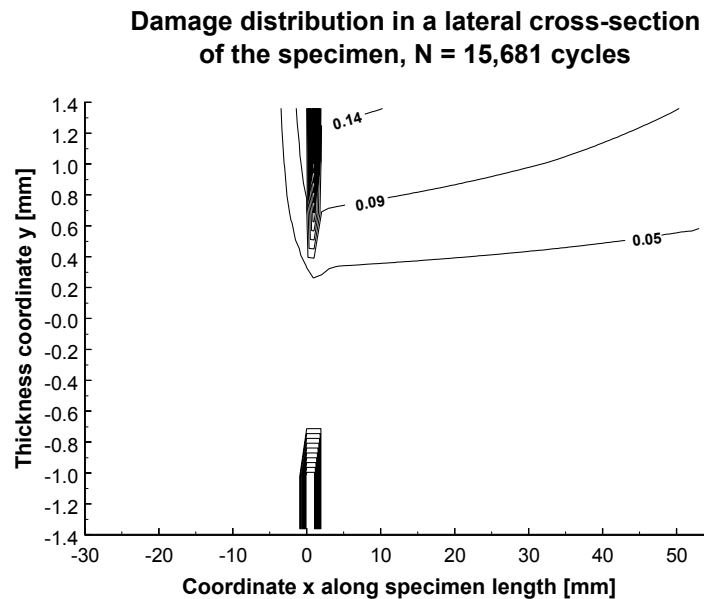


Figure 16 Damage distribution in a lateral cross-section of the specimen at N = 15,681 cycles.

As the damage distribution in Figure 16 corresponds with final failure of the composite component, this damage distribution is compared against the experimental micrographs which were recorded at the end of the fatigue test.

Figure 17 shows the optical micrograph of the specimen at the clamped cross-section. The position of the clamping fixtures and the direction of the bending moment $M(x)$ have been schematically indicated.

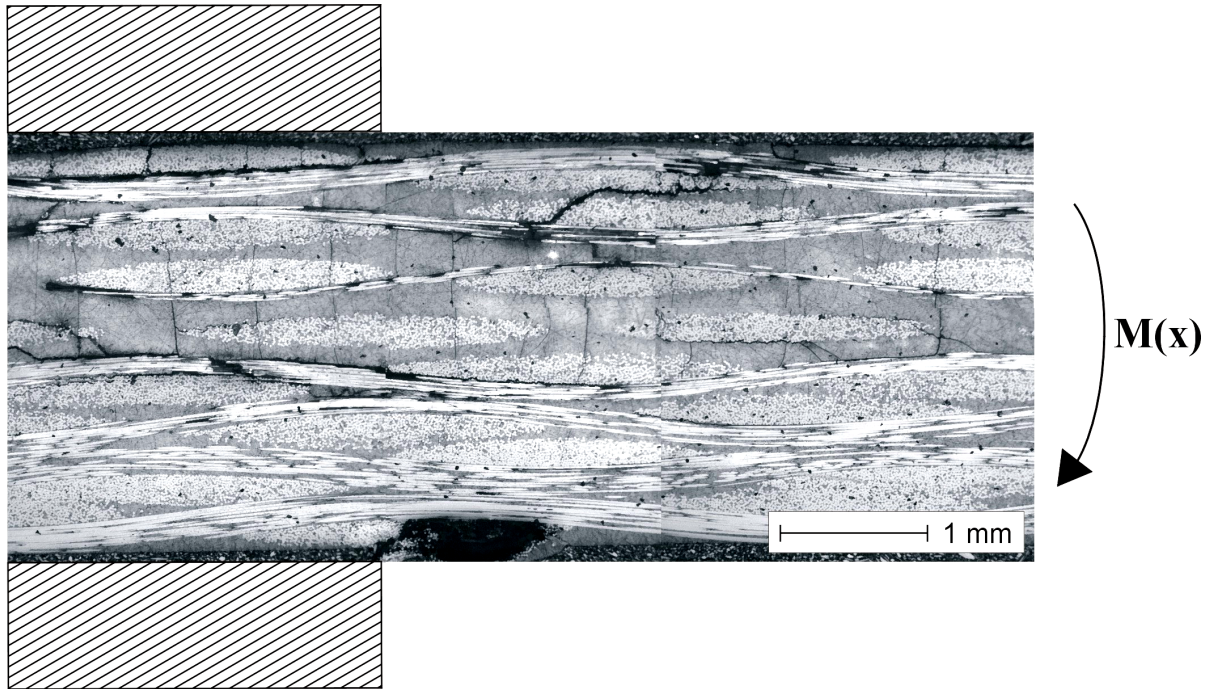


Figure 17 Optical micrograph at the clamped cross-section.

There appears to be a very good agreement between the damage distributions of Figure 16 and Figure 17. The predicted damage distribution at the compressive side is very narrow, only about 2 millimeters in width. This is confirmed by the micrograph, where the matrix is completely shattered over a small length at the compressive side. However this damage does not propagate into the inner area of the composite specimen. The length scale is indicated and can be compared with the full thickness of the specimen, being 2.72 mm.

At the tensile side, the predicted damage distribution is smeared out over a large width and the zone of moderate to severe damage can be estimated to be about 10 millimeters in width (see Figure 16). This compares very well with the experimental observations, as can be seen on a more global view of the lateral cross-section of the composite specimen in Figure 18.

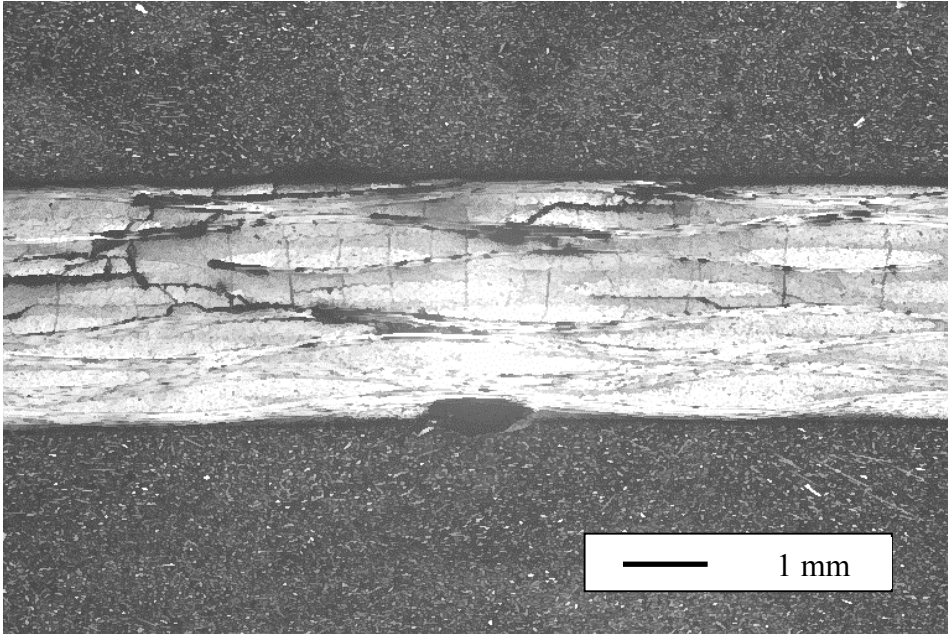


Figure 18 Global view of the lateral cross-section near the clamped fixation.

Away from the fixation, the finite element simulation still predicts damage values of 5 % to 9 % at the tensile surface of the specimen (see Figure 16). This damage can be clearly seen on the following picture giving a top view of the tensile side of the specimen after the fatigue test “Pr08_2” has been ended.

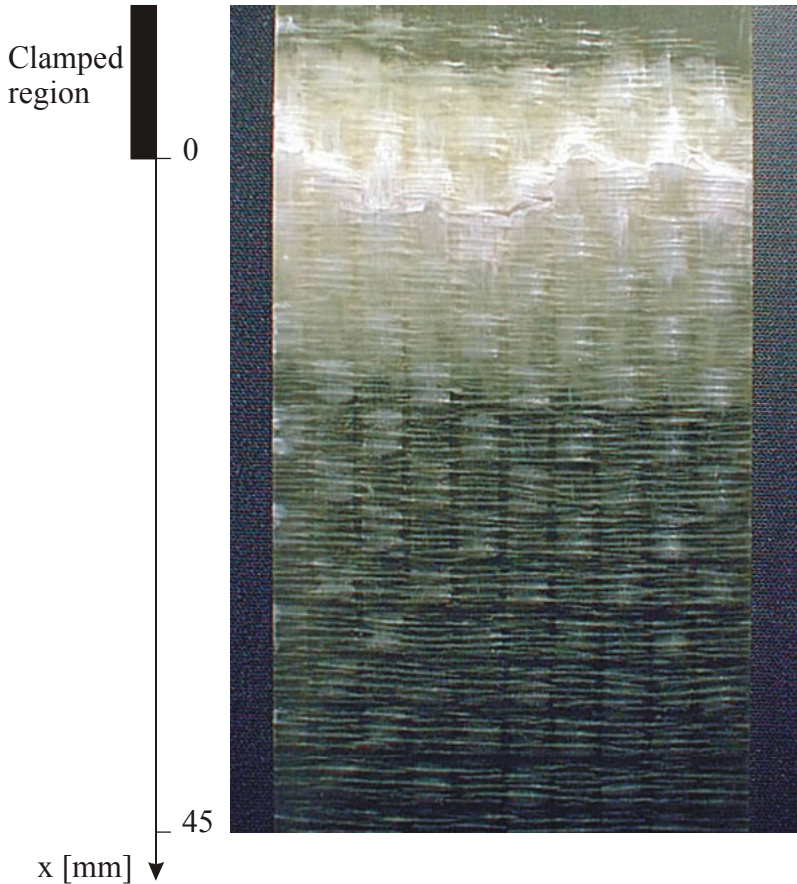


Figure 19 Top view of damage distribution at the tensile side of the specimen.

Several fibres of the $[\#0^\circ]_8$ specimen are broken at the clamped end of the specimen and a sort of ‘hinge’ is formed. Further away from the fixation a regular and gradually decreasing pattern of transverse cracking in the weft tows at the fabric cross-over points is shown in the specimen. This ‘characteristic damage state’ is very similar to the steady state matrix cracks in tension fatigue of plain-woven composites [10,11] and corresponds to the predicted damage values of 5 % to 9 %.

7. Conclusions

Based on a residual stiffness approach, a fatigue damage model has been proposed. Through a modified use of the Tsai-Wu static failure criterion, a measure for the reserve to failure has been defined as the “fatigue failure index”, which accounts for the applied nominal stress level and the presence of fatigue damage. The damage growth rate equation has been split up in a damage initiation and a damage propagation term. This combined modelling approach allows for simulation of the three stages in stiffness degradation (sharp initial decline – gradual degradation – final failure).

The fatigue damage model has been implemented in a commercial finite element code. As such, the model could be applied to displacement-controlled bending fatigue tests on plain-woven glass/epoxy specimens. The stress distribution, damage-cycle histories and damage distributions were predicted and compared with experimental observations.

Acknowledgements

The author W. Van Paepegem gratefully acknowledges his finance through a grant of the Fund for Scientific Research – Flanders (F.W.O.), and the advice and technical support of the SAMTECH company. The authors also express their gratitude to Syncoglas for their support and technical collaboration.

References

1.	Degrieck J, Van Paepegem W. Fatigue Damage Modelling of Fibre-Reinforced Composite Materials: Review. <i>Appl Mech Rev</i> 2001;54(4):279-300.
2.	Van Paepegem W, Degrieck J. New coupled approach of residual stiffness and strength for fatigue of fibre-reinforced composites. Eight International Conference on Composites Engineering (ICCE/8). Proceedings, Tenerife, 5-11 August 2001.
3.	Van Paepegem W, Degrieck J. A New Coupled Approach of Residual Stiffness and Strength for Fatigue of Fibre-reinforced Composites. <i>Int J Fatigue</i> (in press).
4.	Schulte K. Stiffness reduction and development of longitudinal cracks during fatigue loading of composite laminates. Mechanical characterisation of load bearing fibre composite laminates. Proceedings of the European Mechanics Colloquium 182, 29-31 August 1984, Brussels, Belgium, Amsterdam:Elsevier. p. 36-54.
5.	Highsmith AL, Reifsnider KL. Stiffness-reduction mechanisms in composite laminates. In: Reifsnider KL, editor. <i>Damage in composite materials</i> . ASTM STP 775. Philadelphia:American Society for Testing and Materials, 1982.

6.	Masters JE, Reifsnider KL. An investigation of cumulative damage development in quasi-isotropic graphite/epoxy laminates. In: Reifsnider KL, editor. <i>Damage in composite materials</i> . ASTM STP 775. Philadelphia: American Society for Testing and Materials, 1982.
7.	Sol H, de Wilde WP. Identification of elastic properties of composite materials using resonant frequencies. <i>Proceedings of the International Conference "Computer Aided Design in Composite Material Technology"</i> , Southampton, Springer-Verlag, 1988. p. 273-280.
8.	Sol H. Identification of the complex moduli of composite materials by a mixed numerical/experimental method. <i>Proceedings of the second International Conference on Computer Aided Design in Composite Material Technology</i> , Brussels, Springer-Verlag, 1990. p. 267-279.
9.	Van Paepegem W, Degrieck J, De Baets P. Finite Element Approach for Modelling Fatigue Damage in Fibre-reinforced Composite Materials. <i>Compos Part B</i> 2001;32(7):575-588.
10.	Fujii T, Amijima S, Okubo K. Microscopic fatigue processes in a plain-weave glass-fibre composite. <i>Comp Sci Tech</i> 1993;49:327-333.
11.	Manger CIC, Ogin SL, Smith PA, Greaves RP. Damage development in plain weave GFRP. <i>Proceedings of the Eleventh International Conference on Composite Materials (ICCM/11)</i> , Gold Coast, Queensland, Australia, Woodhead Publishing Limited, 1997. p. V.58-V.66.